Electrochimica Acta 384 (2021) 138299

Contents lists available at ScienceDirect

Electrochimica Acta

journal homepage: www.elsevier.com/locate/electacta

Co_9S_8 nanoparticles embedded in nitrogen, sulfur codoped porous carbon nanosheets for efficient oxygen/hydrogen electrocatalysis

Xiaojing Zhu[a], Qikai Wu[a], Jiale Dai[a], Dengke Zhao[a], Chenghao Yang[a], Ligui Li[a,b,*], Nanwen Li[c], Shaowei Chen[d]

[a] Guangzhou Key Laboratory for Surface Chemistry of Energy Materials, New Energy Research Institute, School of Environment and Energy, South China University of Technology, Higher Education Mega Center, 382 East Waihuan Road, Guangzhou 510006, China
[b] Guangdong Provincial Key Laboratory of Advance Energy Storage Materials, South China University of Technology, Guangzhou 510640, China
[c] State Key Laboratory of Coal Conversion, Institute of Coal Chemistry, Chinese Academy of Sciences, Taiyuan 030001, China
[d] Department of Chemistry and Biochemistry, University of California, 1156 High Street, Santa Cruz, California 95064, USA

ARTICLE INFO

Article history:
Received 6 February 2021
Revised 29 March 2021
Accepted 30 March 2021
Available online 11 April 2021

Keywords:
Carbon-based electrocatalyst
Organometal complex
Selective ethcing
Oxygen/hydrogen electrocatalysis

ABSTRACT

Directly pyrolyzing organometal complex represents a judicious strategy to fabricate efficient multifunctional carbon-based electrocatalysts, but the structure/composition of the catalysts is commonly complicated and the corresponding electrocatalytic activities are usually compromised. In this study, we report a selective leaching route to prepare small Co_9S_8 nanoparticles supported on nitrogen, sulfur codoped porous carbon nanosheets (Co_9S_8@PNSC) by pyrolyzing sheet-like Co(II)-coordinated thiourea-ethylenediamine-formaldehyde resin (Co-TEFR)/polydopamine (PDA) hybrids that are covered by silica shell layer, followed by removal of the silica and Co nanoparticles with NH_4HF_2 through a wet etching method. Consequently, the resultant Co_9S_8@PNSC exhibits high specific surface area, hierarchical porosity and tiny Co_9S_8 nanoparticles, which are conducive to the maximal utilization of active sites, endowing remarkable oxygen electrocatalysis with a half-wave potential of +0.845 V for oxygen reduction reaction and a low overpotential of 314 mV at current density of 10 mA cm^{-2} for oxygen evolution reaction. Besides, such composite also shows a considerable electrocatalytic performance for hydrogen generation. When applied in an assembled zinc-air battery, Co_9S_8@PNSC displays a high power-density (203 mW cm^{-2}) and favorable cycling lifespan. The results from the present strategy may provide an exemplification in rational design and fabrication of carbon-based nanocomposite for high-performance multifunctional electrocatalysis.

1. Introduction

Due to their high specific surface area, hierarchical porous textures, cost-effective and good corrosion resistance [1–4], porous carbon-supported transition-metal catalysts have been widely researched to replace high cost noble-metal-based electrocatalysts (e.g. Pt and Ir oxides) in fuel cells and metal–air batteries [5–9]. Recently, pyrolysis of metal-polymer complex is manifested to be an powerful and judicious strategy to construct porous carbon-based nanomaterials for high-performance electrocatalysis [10–14]. For example, Lin et al. reported a simple thermal annealing to fabricate Co_9S_8@CoS@CoO@C nanoparticles as hihgly efficient electrocatalysts for oxgen evolution by using a three-dimensional diamondoid framework Co-MOF as precursor [15]. Han et al. synthesized hierarchical porous tubular nanostructures composed of core-shell nanoparticles with Co-Co_9S_8 as core and N, S codoped carbon (Co-Co_9S_8@SN-CNT) as shell as a trifunctional catalyst for hydrogen/oxygen electrocatalysis by using one-dimensional cobalt-based metal organic framework as self-template precursor [16]. Likely, we also reported an efficient bifunctional oxygen electrocatalyst composed of cobalt-based nanostructured metal phases (Co, Co_3O_4 and CoS_x particles) supported on N, S codoped porous carbon submicrospheres (Co-NTMCs@NSC) through pyrolysis of the organometal precursor of Co(II)-chelated thiourea-ethylenediamine-formaldehyde resin and polydopamine (Co-TEFR@PDA) [17]. Although remarkable electrocatalysis has been made, it always causes the formation of different metal nanoparticles mixture embedded in porous carbon, which may suffer from the challenges of compromised individual performance or even selective removal of inert metal nanoparticles, leading to the loss of the catalytic activity and concurrently complicating the fundamen-

* Corresponding author.
E-mail address: esguili@scut.edu.cn (L. Li).

https://doi.org/10.1016/j.electacta.2021.138299
0013-4686/

tal research [18]. Furthermore, the development of a single electrocatalyst that integrates trifunctional catalytic activities for oxygen reduction reaction (ORR), oxygen evolution reaction (OER), and hydrogen reduction reaction (HER) is significant to effectively simplify the components integration and markedly reduce fabrication cost.

Herein, we develop a selective leaching method to synthesis Co_9S_8 particles incorporated in nitrogen, sulfur codoped porous carbon nanosheets (Co_9S_8@PNSC) by the pyrolysis of the assembled hybrid of silica, Co(II)-chelated thiourea-ethylenediamine-formaldehyde resin (Co-TEFR) and polydopamine (PDA), and the followed etching treatment with NH_4HF_2. In this process, the novel etching reagent could remove the silica and selectively etch the Co particle in the hybrid-derived precursor, silica-containing and Co/Co_9S_8 particles embedded carbonaceous nanosheet (silica-Co/Co_9S_8@PNSC), achieving the final catalyst Co_9S_8@PNSC with high specific surface area, abundant hierarchical porosity and active nanoparticles. As a consequence, the resultant nanocomposite exhibits highly efficient ORR activity ($E_{1/2}$ = +0.845 V) and remarkable electrocatalysis toward oxygen/hydrogen production with overpotential of 314 mV for OER and 192 mV for HER at 10 mA cm^{-2} in alkaline media, comparable to and even superior to the catalytic activity of other trifunctional electrocatalysts reported in recent literature (Table S1). When applied as air−cathode for Zn−air batteries, the Co_9S_8@PNSC-assembled device shows a higher power density (203 mW cm^{-2}) and better cycling stability than commerical Pt/C-based one.

2. Experimental section

2.1. Materials

Thiourea (99%), tetraethyl orthosilicate (99.99%), cobalt nitrate hexahydrate (99%), ethylenediamine (99.5%), formaldehyde solution (37%) and dopamine hydrochloride (98%) were purchased from Aladdin. All reagents were analytical grade and utilized as received without any purification.

2.2. Preparation of Co_9S_8@PNSC

Brieftly, 0.5 g of thiourea (TU) and 0.2 g of $Co(NO_3)_2$•$6H_2O$ were dissolved in 40.0 mL of deionized water to obtain a clear and transparent solution, followed by the solw addition of 0.40 mL of ethylenediamine (En) and 1.44 mL of formalin (CH_2O, 37 wt.%) under vigorous stirring at atmosphere temperature. Subsequently, 5.0 mL of dopamine aqueous solution (40.0 mg mL^{-1}) was immediately added into the above mixture with magnetic stirring for 2 h. Next, 0.2 mL of tetraethyl orthosilicate (TEOS) was added drop and drop. Upon further stirring for 24 h, the precipiate in the reaction mixture was obtained by centrifugation, and then sequentially purified with ultrapure water and alcohol. Subsequently, the dry precipitate was calcined at 800°C in Ar/H_2 atmosphere to afford the composite (denoted as silica-Co/Co_9S_8@PNSC). Finally, silica-Co/Co_9S_8@PNSC was soaked in 4.0 M NH_4HF_2 aqueous solution at room temperature to leach silica and concurrently selectively remove Co particles, leading to the final product Co_9S_8@PNSC. For comparison, control samples Co/CoO/CoS_x@PNSC and PNSC were preparation in the same manner either without the addition of TEOS or leaching with 10 wt.% HF in deionized water, respectively.

2.3. Electrochemistry

A CHI 750E electrochemical workstation (CH Instruments, Inc., China) was utilized to carry out electrochemical experiments. The ORR measurements were performed within a standard three-electrode configuration using a rotating ring-disk electrode (RRDE) as working electrode. An Ag/AgCl electrode and Pt foil were empolyed as the reference and counter electrodes, respectively. All potentials calibrated by the Ag/AgCl electrode were converted to reversible hydrogen electrode (RHE). Prior to measurement, a homogeneous catalyst ink with a 2.0 mg mL^{-1} of concentration was prepared by the dispersion of as-prepared sample into 1 mL of Nafion/ethanol (0.05 wt.%) solution under ultrasonication treatment. The ink was then dropcast onto the GEC surface and dried under ambient conditions. The catalyst loading on the GCE was 204 μg cm^{-2} unless otherwise indicated. In ORR measurement, linear sweep voltammetry (LSV) was determined in oxygen-saturated 0.1 M KOH electrolyte at a potential sweep rate of 10 mV s^{-1} under different electrode rotation rates of 400 to 2500 rpm. The long-term durability was detected at +0.50 V at 900 rpm rotation speed via amperometric i–t curve. Furthermore, the electron transfer number (n) and the corresponding H_2O^- yield were determined by Eqs. (1) and (2), respectively.

$$n = \frac{I_{Disk}}{I_{Ring}/N + I_{Disk}} \quad (1)$$

$$H_2O^- = \frac{200 I_{Ring}/N}{I_{Ring}/N + I_{Disk}} \quad (2)$$

where N is the current collection efficiency on RRDE (0.37 in the present work) and I_{Disk} and I_{Ring} are referred to the disk and ring currents, respectively.

As for electrochemical OER and HER measurements, catalysts loaded on carbon cloth (0.25 cm^2) and an Ag/AgCl electrode with saturated KCl were utilized as the working and reference electrodes, respectively. Whereas, Pt foil and carbon rod were employed as the counter electrode for OER and HER measurements, respectively. The catalyst loading was set at 0.404 mg cm^{-2}. All LSVs were recorded in 1 M KOH electrolyte with a scan rate of 10 mV s^{-1}. Electrochemical impedance test was conducted at +1.55 V and −0.280 V for OER and HER, respectively, with an AC amplitude of 5 mV from the frequency range of 10^5 Hz to 0.01 Hz. Unless stated otherwise, all the potentials for OER and HER are referred to RHE and have been iR-corrected according to the following equation:

$$E_{compensated} = E_{measured} - iR_u$$

where $E_{compensated}$ is iR-corrected potential, $E_{measured}$ is experimentally measured potential, and R_u is the compensated resistance.

2.4. Rechargeable Zn–Air battery

Rechargeable Zn–air battery was assembled by employing a polishing zinc plate as the anode, and the composite loaded on the hydrophobic side of carbon cloth was utilized as a breathable electrode and an aqueous solution containing 6.0 M KOH and 0.2 M $Zn(Ac)_2$•$2H_2O$ was filled as working electrolyte. Prior to the homemade device, 3.0 mg mL^{-1} of ink was prepared by the dispersion of electrocatalyst into Nafion/ethanol solution (0.5 wt%) under sonication. Subsequently, the above ink was dropcast onto hydrophobic carbon cloth to achieve breathable electrode with the electrocatalyst loading of 2.0 mg cm^{-2}.

2.5. Characterization

SEM and TEM measurements were conducted on a ZEISS field-emission electron microscope and a Tecnai G2-F20 microscope with the equipment of an energy-dispersive X-ray spectroscopy (EDS) detector, respectively. XRD profiles were recorded on a Bruker D8 instrument with Cu Kα radiation. XPS measurements were conducted on a Phi X-tool instrument. The BET surface area

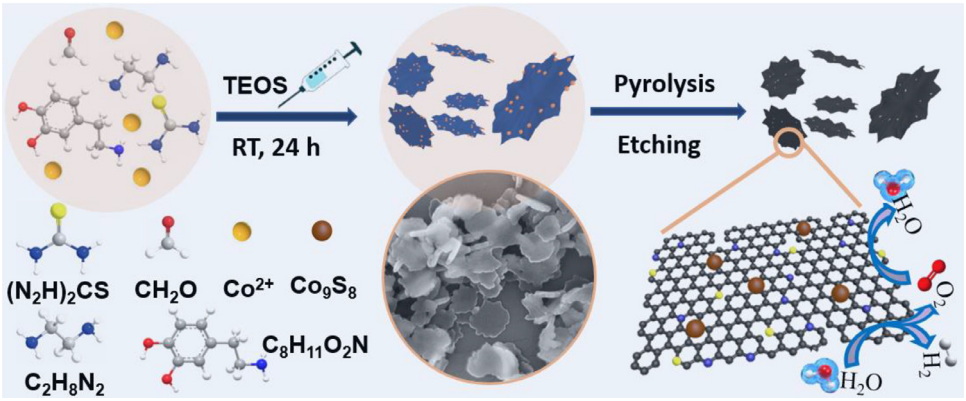

Scheme 1. schematic diagram for illustrating the preparation of Co_9S_8@PNSC.

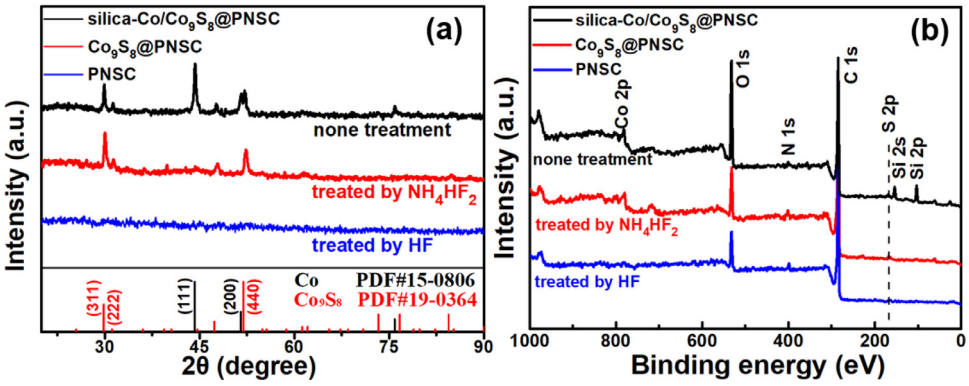

Fig. 1. (a) XRD profiles and (b) XPS survey spectra for various samples with different post treatment.

and the corresponding pore size distribution was defined by measuring N_2 isotherms at 77 K on a Micromeritics ASAP 2010 instrument. Raman spectrum was acquried with a RENISHAW in Via instrument using an Ar laser source.

3. Results and discussion

It should be mentioned that, in our previous study, the coordinated polymer could be assembled with polydopamine to form spherical composite [17]. Interestingly, as shown in Figure S1, the morphology of the coordinated polymer Co-TEFR can be changed into quasi-circular structure with rough edge and multi-heteroatoms by increasing the feeding amount of ethylenediamine, which acts as a strong alkalinity supplier, chelates with metal ions and results in other formation pathway [19,20]. Regarding the advantage of two-dimension carbon nanosheet (e.g. high specific surface area, enhanced accessible active site and rapid mass/charge transfer), the resultant carbon-based electrocatalyst derived from the sheet-like composite may exhibit extraordinary electrocatalytic performance [21–23]. This consideration is the motive of the present work.

The synthesis process of the typical sample Co_9S_8@PNSC is schematically shown in Scheme 1, where composite nanosheet precursor is firstly fabricated by cooperative assembly of sheet-like Co-thiourea-ethylenediamine-formaldehyde resin (Co-TEFR), polydopamine (PDA) and tetraethyl orthosilicate (TEOS) [24]. Subsequently, the assembled composites are pyrolyzed in Ar/H_2 atmosphere at 800 °C for 2 h and then etched by 4 M NH_4HF_2 to obtain the final product Co_9S_8@PNSC.

During the post treatment, different etching agents (HF and NH_4HF_2) are used to remove the inert constituent such as silica template. The resultant materials are firstly characterized by XRD profiles. As shown in Fig. 1a, the metallic Co (PDF#15-0806) and crystalline Co_9S_8 nanoparticles (PDF#19-0364) are observed for the pristine sample silica-Co/Co_9S_8@PNSC without etching while the Co_9S_8 nanocrystalline is only identified in Co_9S_8@PNSC etching by NH_4HF_2. However, after post treatment by HF, no diffraction peak is found in PNSC, which can also be supported by TEM image (Fig. S2). In addition, XPS survey spectra of different samples are also investigated in Fig. 1b, where the silica peak is obviously identified for the pristine sample silica-Co/Co_9S_8@PNSC while the Co electron is not detected in the PNSC, signifying the selective etching of NH_4HF_2 for metal Co besides silica template. These findings can be further supported by N_2 adsorption/ desorption isotherm measurement (Fig. S3), in which the dominated mesopore sizes and extra specific surface area can be produced by the etching of silica template and metal nanoparticles. Specifically, Co_9S_8@PNSC shows a BET surface area up to 886 $m^2\ g^{-1}$, as listed in Table 1, which is somewhat smaller than that of PNSC (1197 $m^2\ g^{-1}$) but larger than that of silica-Co/Co_9S_8@PNSC (295 $m^2\ g^{-1}$). The extra BET area and the reserved Co_9S_8 nanoparticles may remarkably facilitate to the electrolyte diffusion and electrocatalytic activity, respectively [25–27].

The SEM image of the precursor composite silica-Co-TEFR@PDA is shown in Fig. 2a, where the circular-like nanosheet with uniform size and high dispersity can be clearly observed. After carbonization and post treatment, the Co_9S_8@PNSC retains a similar circular-like nanosheet with the average diameter of ~220 nm and thickness of ~30 nm (Fig. 2b and c). These findings can be further visualized by TEM images in Fig. 2d, where the thickness of the nanosheet is in the range of 27 ~ 31 nm. Furthermore, in the TEM image with high magnification (Fig. 2e), one can see that the abundant porous structure and ultrasmall dark spot which is assigned to Co_9S_8 nanoparticles for Co_9S_8@PNSC. Meanwhile, in HR-

Table 1
Summary of texture parameters and atomic fraction of different samples.

Sample name	N_2 adsorption-desorption				EDS Elemental content (at.%)				
	S_{BET} (m^2 g^{-1})	S_{micro}/ S_{ext}[a] (m^2 g^{-1})	V_{total}[b] (cm^3 g^{-1})	D_p[c] (nm)	C	N	O	S	Co
Co/CoO/CoS_x@PNSC	578	395/ 183	1.883	2.6	85.23	1.25	6.95	2.55	4.02
Co_9S_8@PNSC	886	417/ 469	2.311	3.0, >50	69.90	2.07	21.12	3.27	3.64
PNSC	1197	604/ 593	3.004	3.1, 7.3, >50	91.93	3.61	3.66	0.72	0.08

[a] S_{micro}/ S_{ext}: micropore area/ external surface area calculated by using t-pot model.
[b] V_{total}: total pore volume estimated from the adsorbed amounts at $P/P_0 = 0.99$.
[c] *Dp*: predominant pore size distribution determined by BJH model.

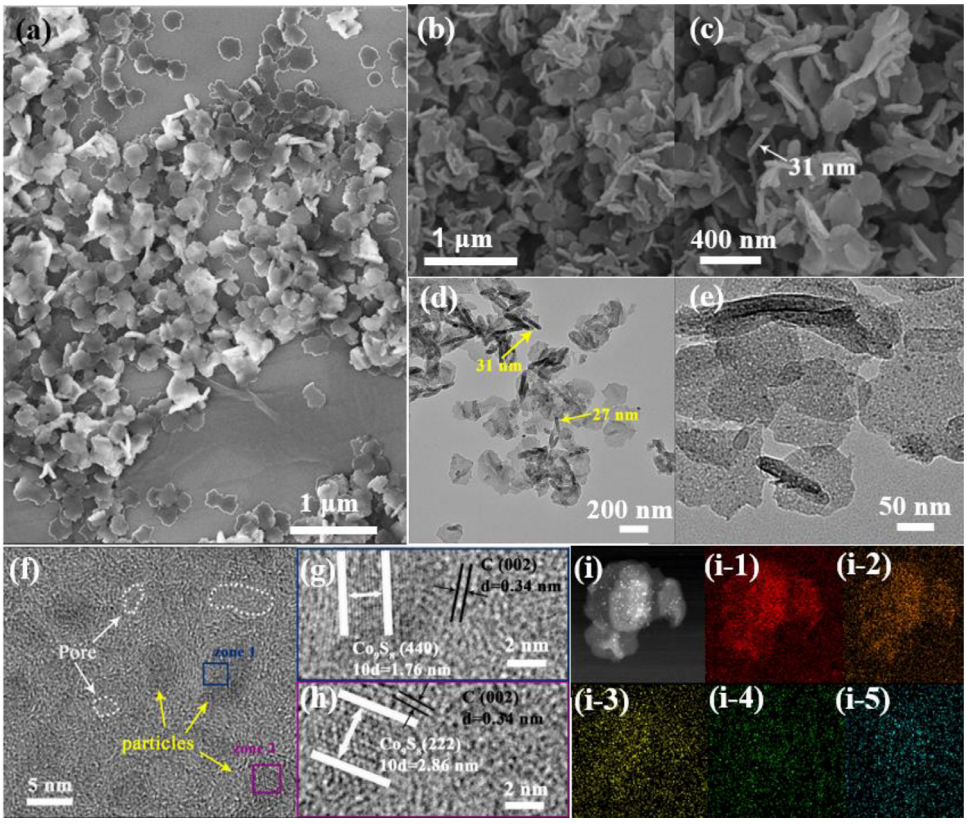

Fig. 2. Representative SEM images of (a) the precursor silica-Co-TEFR@PDA and (b, c) the corresponding carbonized sample Co_9S_8@PNSC. (d, e, f) TEM images of Co_9S_8@PNSC. (g, h) HR-TEM images for the selective region of Fig. (f); The selected-area EDS elemental maps of (i-1) C, (i-2) N, (i-3) O, (i-4) S and (i-5) Co.

TEM image (Fig. 2f), the dominated pore sizes are determined to be ~3 nm while the metal nanoparticle sizes are measured to be ~5 nm. Besides, in the corresponding HR-TEM images of the selective region (Fig. 2g and h), lattice fringes with an interspacing of 0.176 and 0.286 nm are well resolved, in agreement with the (440) and (222) planes of crystalline Co_9S_8, respectively. Meanwhile, the short-range defective graphite layer structure can be clearly found in the region close to Co_9S_8 nanoparticles. In addition, elemental mapping measurements (Fig. 2i) reveal the even distribution of C, N, O, S and Co elements on the sheet-like catalyst. Apart from the electrocatalytic activity of defective structure, the two-dimensional sheet and porous textures are advantageous to the accessibility to active sites and the transportation of intermediate products, while Co_9S_8 nanoparticles with small sizes can also serve as catalytic sites which plays a positive impact on electrocatalysis [28].

In order to investigate the influence of TEOS on the formation of this circular-like porous carbon nanosheet containing Co_9S_8 nanoparticles, a control sample, N, S codoped porous carbonaceous nanosheet containing metallic Co particles (referred to Co/CoO/CoS_x@PNSC), was prepared without the addition of TEOS. It should be noted that, in the absence of TEOS, the obtained sample exhibits a similar sheet-like morphology but the sizes and structure of the particles are changed into 30 nm and the mixture crystalline of Co and CoO as well as graphite layers, respectively (Fig. S4a-d). However, the metallic Co particles are still detected and remained in the counterpart after the same etching manner by NH_4HF_2 (Fig. S5), which is mainly due to the protection of graphite carbon for the particles [29]. Combing the TEM findings, it can be reasonably concluded that the addition of TEOS not only effectively confines the aggregation of metal nanoparticles, but plays a crucial role in achieving the particles crystalline and defective graphitic layers [30,31], both of which are significant to boost electrocatalysis [30].

Fig. 3a shows the Raman spectrum of Co_9S_8@PNSC which possess two distinct peaks of D and G bands. The G band at 1592 cm^{-1} refers to the E_{2g} mode in graphitic carbon materials, while D band is derived from the A_{1g} mode for defective carbons [32].

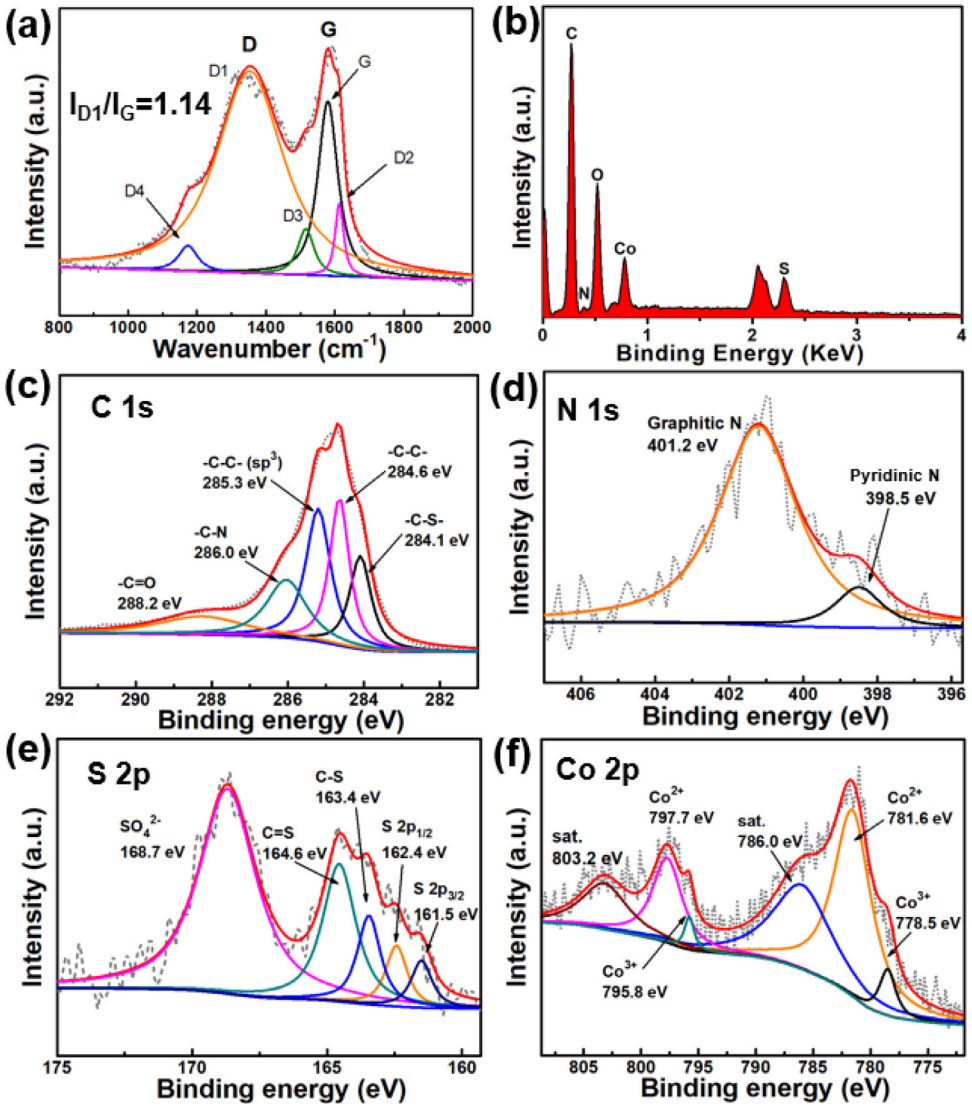

Fig. 3. The typical nanocomposite Co_9S_8@PNSC: (a) Raman spectrum and (b) EDS spectrum, the core-level XPS spectra of (c) C 1s, (d) N 1s, (e) S 2p, and (f) Co 2p electrons.

Furthermore, the D band can be fitted into four peaks by Gaussian-Lorentzian numerical simulation, in which the D peak is wide and the ratio of I_{D1}/I_G is 1.14, indicative of the existence of disordered graphite lattice in the carbon-based material [33]. The findings are well consistent with the HR-TEM result. The defective structure can modulate the electronic and surface properties of the catalysts, mainly facilitating an improved electrocatalysis [34–36]. Besides, from the EDS spectrum of the typical sample Co_9S_8@PNSC depicted in Fig. 3b, in which the C, N, O, S and Co elements are obviously resolved and the coressponding atomic fraction is listed in Table 1. XPS technique is further employed to identify the surface composition of the nanomaterials. As shown in Fig. 4a, deconvolving the core-level XPS spectrum of C 1s electron for Co_9S_8@PNSC yields five peaks at 284.1, 284.6, 285.3, 286.0 and 288.2 eV, corresponding to C–S [37], C=C (sp^2), C–C (sp^3) [38], C–N and C=O species. The formation of C–S moiety further demonstrates that the S heteroatoms are successfully retained in carbon matrix. As for deconvolution of the core-level XPS spectrum of N 1s electron (Fig. 3d), dominated two peaks are in the range beween 396.0 and 402.0 eV, corresponding to pyridinic N (~398.2 eV) and graphitic N (~401.1 eV) [39–42]. The core-level XPS spectrum of O 1s electron (Fig. S6) can be fitted into C=O (531.1 eV), C–O–C (532.1 eV) and C–OH (533.1 eV), indicative of the absence of Co–O species. Beides, S 2p XPS spectrum (Fig. 2e) can be deconvoluted into five well-defined peaks at 161.5, 162.4, 163.4 164.6 and 168.7 eV, which are assigned to the S $2p_{1/2}$, S $2p_{3/2}$, C–S, C=S and the SO_4^{2-} derived from surface oxidation, respectively. In Fig. 3f, the deconvolution fitting of Co 2p electron gives three pairs of peaks, among which the peaks at 778.5 and 795.8 eV may be ascribed to Co^{2+}, while a pair of peaks at 781.6 and 797.7 eV may orignate from Co^{3+}, as well as the rest located at 786.0 and 803.2 eV are satellite peaks. According to the integrated peak areas, the molar ratio of Co^{2+}/Co^{3+} is calculated to be ~8.9, implying the successful reservation of the Co_9S_8 nanoparticles in the carbonaceous materials after etching treatment by NH_4HF_2.

The catalytic activities of the nanocomposites toward ORR are first evaluated by linear scanning voltammetry (LSV). As shown in Fig. 4a, all catalysts show an abrupt current increase, indicating the remarkable performance toward oxygen reduction. However, the half-wave potential vary among different catalysts, at +0.845 V for Co_9S_8@PNSC, +0.832 V for Co/CoO/CoS_x@PNSC, and +0.770 V for PNSC. Hence, it can be found that the PNSC with defective structure and N, S dopants possesses obvious ORR performance while the leaching of Co_9S_8 results in the deterioration of ORR performance, suggesting that the Co_9S_8 particles and the defec-

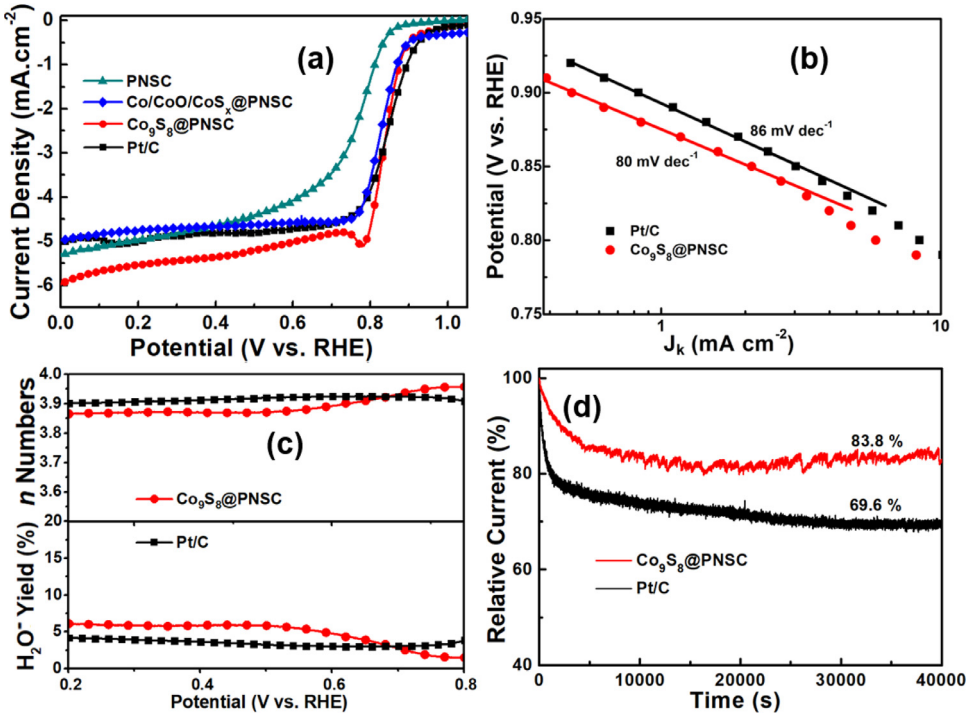

Fig. 4. (a) LSV curves of different catalysts with 1600 rpm rotation speed at 10 mV s^{-1}. (b) Tafel plots for Co_9S_8@PNSC and Pt/C. (c) The plots showing the electron transfer number and H_2O^- yield for Co_9S_8@PNSC and Pt/C. (d) *i*–*t* chronoamperometric curves of Co_9S_8@PNSC and commercial Pt/C catalysts at +0.50 V.

tive carbonaceous structure have a positive impact on the catalytic ORR activity. Previous literature have been reported that the defective carbon structure near to metal particles has a charge polarization for the promotion of the electrocatalytic process [43]. Hence, it may be reasonably concluded that the remarkble ORR catalytic activity of Co_9S_8@PNSC mainly originate from the synergistic effect of the heteroatoms-doped and defect carbon and Co_9S_8 particles. The ORR measurement indicate the best electrocatalytic activity for Co_9S_8@PNSC, much comparable to that of Pt/C electrode (+0.847 V). Nevertheless, Co_9S_8@PNSC displays a remarkble limiting current density of 5.221 mA cm^{-2} at +0.500 V, as compared to Pt/C catalyst (4.80 mA cm^{-2}). Besides, the cathodic current of Co_9S_8@PNSC close to +0.800V shows a distinct tendency to abruptly increased and then fall, which mainly ascribe to the existence of abundant interconnected porosity caused by the etching of metallic Co and the gap of the aggregation of circular-like nanosheet [44]. The corresponding Tafel plots are depicted in Fig. 4b, in which the slopes are calculated to be 80 and 86 mV dec^{-1} for Co_9S_8@PNSC and Pt/C, respectively. These highly comparable slopes suggest that the reaction kinetic on the Co_9S_8@PNSC is analogous to that proceeding on Pt/C during ORR electrocatalysis, that is, the first-electron reduction of oxygen dominates the entire ORR kinetics [45].

Fig. 4c shows the electron transfer number (n) and the generated peroxide species (H_2O^-) yields for the typical sample Co_9S_8@PNSC and commercial Pt/C. It can be observed that the n values of Co_9S_8@PNSC sample is close to 4 over a definite potential region from +0.2 to +0.8 V, even higher than that of Pt/C at high potential region such as +0.75 V, implying a higher selectivity toward $4e^-$ reduction of oxygen for Co_9S_8@PNSC. Similarly, the H_2O^- yield of Co_9S_8@PNSC is very clese to that of Pt/C, confirming that Co_9S_8@PNSC material could serve as an efficient catalyst toward ORR. What's more, the corresponding Koutecky-Levich plots for Co_9S_8@PNSC and commercial Pt/C (Fig. S7) exhibit a high linear trend in the potential range of +0.570 to +0.730 V, indicating that a first-order reaction kenetics with regard to the oxygen concentration in the electrolyte is adopted. Furthermore, durability of nanocomposite-modified electrode is an crucial parameter for electrocatalysis. Fig. 4d shows the amoperometric *i*–*t* curves with continuous operation for 40000 s. One can find that Co_9S_8@PNSC can maintains 83.8% of its initial current, higher than the commercial Pt/C (69.6%), confirming that Co_9S_8@PNSC possesses higher working stability than Pt/C.

Tolerance to crossover effect is another important issue for evaluating ORR electrocatalysts. On the basis of this consideration, methanol is used as a illustrated fuel to analyze and compare the studies. As shown in Fig. S8, upon the addition of 1 M methanol into electrolyte, one can find that a sharp decrease of current density is observed for the Pt/C electrode while only slight fluctuation and no apparent current change are found for the Co_9S_8@PNSC electrode. Theses results obviously suggest that Co_9S_8@PNSC catalyst possess a higher tolerance to crossovered methanol than Pt/C.

Previous literatures have been reported that the metallic Co_9S_8 composites can efficiently catalyze ORR and OER [46–48]. Hence, the OER activity of different samples are investigated in 1 M KOH electrolyte. As shown in Fig. 5a, a sharply increase of voltammetric currents are observed for all the investigated samples, suggesting an apparent OER catalytic performance. Specifically, at a current density of 10 mA cm^{-2}, Co_9S_8@PNSC shows the lowest overpotential ($E_{OER,\ 10}$) of only 314 mV, as compared with 418 mV for Co/Co_9S_8@PNSC, 519 mV for PNS and 323 mV for IrO_2 catalyst. Additionally, from the corresponding Tafel plots depicted in Fig. 5b, Co_9S_8@PNSC shows a moderate slope of 169 mV dec^{-1}, a value that is higher than that of IrO_2 (102 mV dec^{-1}), but lower than the 171 mV dec^{-1} for Co/Co_9S_8@PNSC and 191 mV dec^{-1} for PNSC. Furthermore, comparison with the typical sample Co_9S_8@PNSC, the PNSC catalyst with removal of the Co_9S_8 nanoparticles lost the prominent OER activity, directly proving that Co_9S_8 nanoparticles are benefcial for promoting OER electrocatalytic activities. Additionally, the key parameters of overpotential and Tafel plots for different catalysts toward OER are summarized in Fig. 5c for compar-

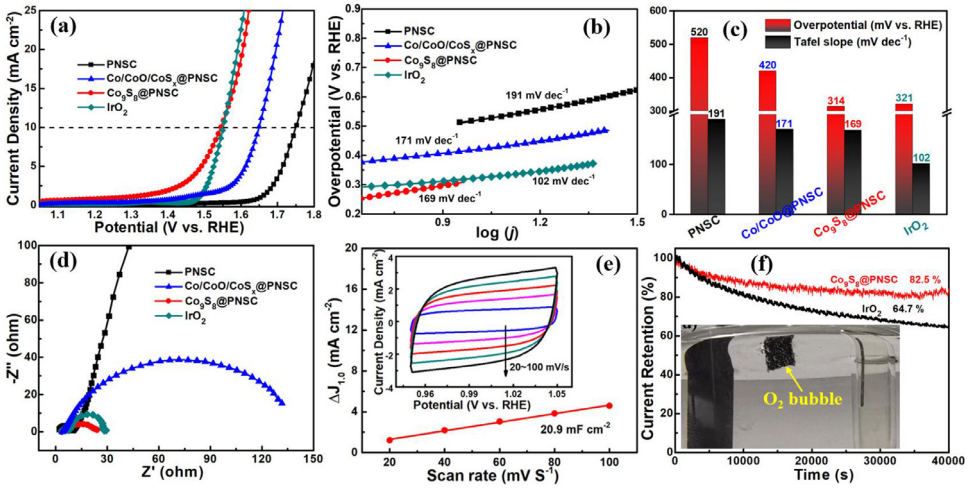

Fig. 5. (a) OER LSV curves. (b) The corresponding Tafel plots. (c) Histogram showing the $E_{OER,\ 10}$ and Tafel plots. (d) Electrochemical impedance spectra. (e) Double-layer capacitance for Co_9S_8@PNSC; inset the panel shows a series of CV curves for Co_9S_8@PNSC with vairous sweep speed of 20 to 100 mV s^{-1} at different potential region from +0.950 to 1.050 V. (f) *i–t* chronoamperometric response of Co_9S_8@PNSC and commercial IrO_2 electrocatalyst, Inset to the panel is optical photograph showing the production of O_2 bubbles on Co_9S_8@PNSC-modified electrode during chronoamperometric measurement. All potentials have been iR corrected after electrochemical impedance spectra meaurement.

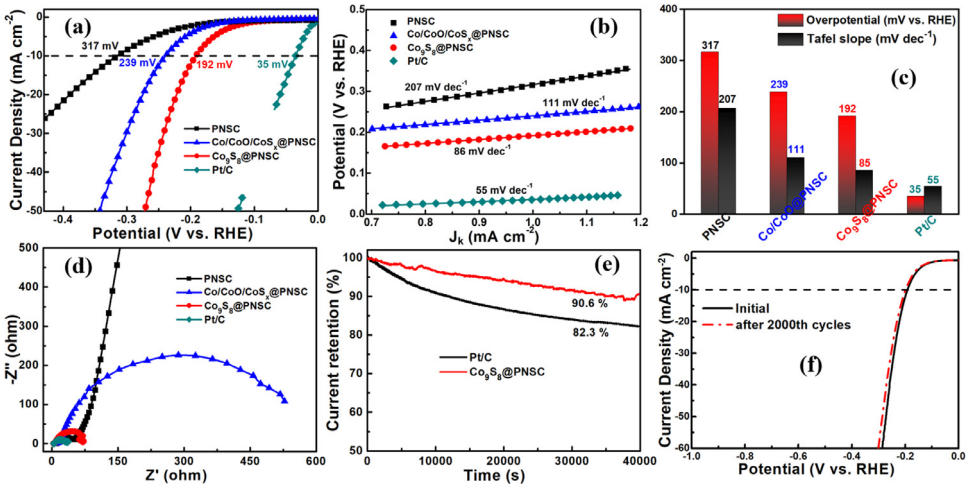

Fig. 6. (a) HER LSV curves of different catalysts. (b) The corresponding Tafel plots. (c) Histogram showing the key parameter for a series of catalysts. (d) Electrochemical impedance spectra. (e) *i–t* chronoamperometric response of Co_9S_8@PNSC and Pt/C. (f) LSVs of Co_9S_8@PNSC before and after 2000 cycles. All potentials have been iR-corrected.

ison, visually demonstrating the remakable OER electrocatalysis for Co_9S_8@PNSC among the series.

Besides, charge transfer resistant (R_{ct}) is effectively estimated to elucidate the OER catalytic kinetics of different catalysts through electrochemical impedance test. As shown in Fig. 5d, the smallest semicircle is observed for Co_9S_8@PNSC than other catalysts Co/Co_9S_8@PNSC, PNSC and commercial IrO_2 in alkaline electrolyte, indicating the lowest charge transfer resistance for Co_9S_8@PNSC amony these catalysts. To further account for the remakable OER performance for Co_9S_8@PNSC, electrochemical surface area (ECSA) is a significant indicator and estimated by the calculation of the electrochemical double-layer capacitance (C_{dl}) from the CVs at different potential region from +0.950 and +1.050 V. As shown in Fig. 5e and S9, a C_{dl} value of Co_9S_8@PNSC is determined to be 20.9 mF cm^{-2}, much higher than that of Co/Co_9S_8@PNSC (6.4 mF cm^{-2}), and PNSC (16.8 mF cm^{-2}) in 1 M KOH solution. To sum up, Co_9S_8@PNSC electrocatalyst have the lowest charge transter resistance and much larger ECSA, which are advantageous to the electron transpor and the exposure of the electrocatalytically active sites, respectively, endowing the superior OER electrocatalytic performance for Co_9S_8@PNSC. Chronoamperometric response further demonstrates the higher lifespan for Co_9S_8@PNSC than commercial IrO_2 catalyst. From Fig. 5f, after continuous measurement for about 11 h, Co_9S_8@PNSC retained 82.5% of its initial value, while IrO_2 gradually decrease to ~64.7% under the same conditions. The degradation of OER performance for Co_9S_8@PNSC sample is mainly owing to the slow loss of electrocatalysts arising from the peeling effect of accumulated O_2 bubbles on electrode surface (inset to Fig. 5f). Many studies have suggested that Co_9S_8 can gradually transform into cobalt oxyhydrates under OER conditions [49–51], which are the true catalytically active species for the OER. To understand the possible active sites of Co_9S_8@PNSC for the OER, we performed XRD measurement after the chronoamperometric OER test (Fiugre S10), where visible peaks for $Co(OH)_2$ are observed in post-OER Co_9S_8@PNSC. Thus, a cobalt oxyhydrates is more likely to be the actual active species for remarkable OER activity.

Additionally, the catalytic activity of Co_9S_8@PNSC for HER electrocatalysis was further conducted in 1 M KOH electrolyte. As shown in Fig. 6, to afford the current density of 10 mA cm^{-2}, Co_9S_8@PNSC requires an overpotential of 192 mV, which is somewhat larger than the 35 mV for Pt/C but much less than 317 mV

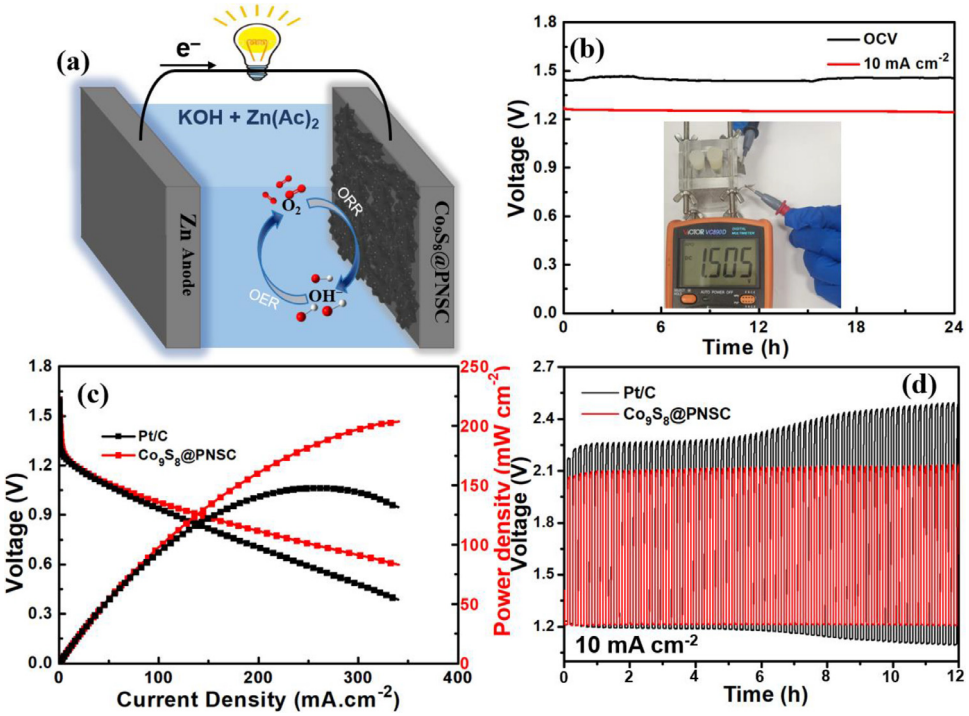

Fig. 7. (a) Sketch for illustrating the configuration of a rechargeable Zn–air battery. (b) plots showing the voltage of Zn–air batteries using Co_9S_8@PNSC as cathode catalysts, while the optical image shows the open circuit voltage by using multimeter. (c) The discharged polarization curves and power density against current density. (d) galvanostatic charge–discharge measurement at 10 mA cm^{-2}.

for PNSC and 239 mV for Co/CoO/CoS_x@PNSC. In addition, From Fig. 6b, the Tafel slope for Co_9S_8@PNSC is determined to be 86 mV dec^{-1}, which is close to that of Pt/C (55 mV dec^{-1}). This observation indicates that the HER process on Co_9S_8@PNSC follow a Volmer–Heyrovsky mechanism [52,53]. The above results can be more clearly presented by the histogram comparison in Fig. 6c. Noted that, the electrocatalytic HER activity of Co_9S_8@PNSC is superior to the PNSC catalyst, obviously demonstrating that Co_9S_8 nanoparticles are advantageous to boost HER performance.

EIS measurements are further conducted to probe the electron transfer property of the electrocatalysts. As shown in Fig. 6d, the typical Co_9S_8@PNSC sample exhibits the smallest semicircle among the series but a slightly higher R_{ct} than that of commercial Pt/C. This finding indicates the favourable charge transfer for Co_9S_8@PNSC, which markedly facilitate the HER process. In addition, the long-term durability is another important criterion to estimate an electrocatalyst performance. It is noteworthy that, after 40,000 s chronoamperometric measurement, as shown in Fig. 6e, 90.6% of relative current density is retained for Co_9S_8@PNSC, which is larger than that of Pt/C (82.3%), signifying the high HER stability of Co_9S_8@PNSC. The superior operational stability can be further supported by accelerated durability test (ADT) in Fig. 6f, where the Co_9S_8@PNSC shows a negligible negative shift after 2000 cycles. Afer the HER, the crystal structure of Co_9S_8@PNSC remains unchanged, as evident from XRD with no apparent variation (Fig. S11), suggesting good durability of the Co_9S_8@PNSC nanomaterial itself under HER conditions.

The OER and HER electrocatalysis of different composites are also conducted in 0.1 M KOH aqueous solutions (Fig. S12), and the corresponding results suggest that the overall OER and HER electrocatalysis activities of present electrocatalysts are more efficient in 1.0 M KOH aqueous solution than those observed in 0.1 M KOH electrolyte.

Consequently, the resultant Co_9S_8@PNSC exhibits efficient ORR activity and remarkable electrocatalysis toward oxygen/hydrogen production in alkaline media, comparable to and even superior to those of the currently reported Co_9S_8-based composites and other trifunctional electrocatalysts (Table S1). Among these literatures, the heteroatoms-doped carbon/ Co_9S_8 hybrids as low-cost electrocatalysts generally show outstanding bifunctional activities [54–57]. Taking a Co_9S_8-based catalyst reported by Gao's work as a typical sample [57], they employed a simple method to fabricate Co_9S_8/N, S codoped honeycomb-structured porous carbon (Co_9S_8/NSC) in situ composites, which was composed of monodisperse Co_9S_8 particles and three-dimensional interconnected network as well as N, S heteroatoms-doped carbon matrix, hence endowing the highly efficient ORR/ OER electrocatalysis of the catalyst. Differently, in this study, a selective etching route is successfully developed to construct a remarkable trifunctional electrocatalyst (Co_9S_8@PNSC), which consisted of small Co_9S_8 nanoparticles with a diameter of about 5 nm (Fig. 3) and heteroatoms-doped defective carbon substrate as well as two-dimensional quasi-circular nanosheet with high specific surface area and hierarchical porosity (Table 1 and Fig. S4). The hierarchical porous architectures with abundant meso-/ macro-pores, derived from the intrinsic mesopore and extra macropore of the gap between the nanosheet, ensure the fast mass transportation and maximum accessibility to the active sites. The ultrafine Co_9S_8 nanoparticles entrapped by N, S codoped and defective carbon allow the improvement of electrical conductivity and maximize the utilization of active sites. These characteristics contribute to the remarkable oxygen/ hydrogen electrocatalysis for Co_9S_8@PNSC.

The above results display that Co_9S_8@PNSC can efficiently catalyzed the ORR and OER [58], which can be applied in oxygen reversible electrocatalysts for rechargeable Zn-air batteries. As illustrated in Fig. 7a, a home-made device of Zn-air battery is fabricated to further investigate the catalytic activity of Co_9S_8@PNSC. In Fig. 7b, the battery using Co_9S_8@PNSC as the air cathode shows an open-circuit voltage of 1.466 V and the discharge potential of 1.255 V at 10 mA cm^{-2}, in which the former is well consistent

with the value determined by using the multimeter. From the discharge polarization curves shown in Fig. 7c, it can be seen that the device with Co_9S_8@PNSC based electrode displays a higher discharge potentials, large than commerical Pt/C-based one at different current densities such as 0.98 V vs. 0.94 V at 100 mA cm^{-2}. Furthermore, the Co_9S_8@PNSC displays a maximum power density of 203 mW cm^{-2}, also much higher than that of Pt/C-modified battery (132 mW cm^{-2}). In addition, the charge–discharge cycles of the catalysts-assembled Zn–air batteries are set at current density of 10 mA cm^{-2} with the intervals for 5 min. As depicted in Fig. 7d, the initial voltage gap of Co_9S_8@PNSC and Pt/C is about 0.852 V and 0.942 V, respectively. After 12 h, the voltage gap is gradually increased to 0.920 V for Co_9S_8@PNSC, much lower than that of Pt/C-assembled device (1.391 V). These observations indicate that a remarkble cycle stability of Co_9S_8@PNSC in rechargeable Zn–air batteries.

4. Conclusions

In summary, nitrogen, sulfur codoped porous carbon nanosheet incorporated with Co_9S_8 particles (Co_9S_8@PNSC) are successfully synthesized by the pyrolysis of the sheet-like composite precursor and followed selective etching treatment with NH_4HF_2. The resulting Co_9S_8@PNSC electrocatalyst comprises abundant porosity and defective graphitic structure as well as catalytically active Co_9S_8 particles, dramatically boosting ORR, OER and HER electrocatalysis. Specifically, Co_9S_8@PNSC displays a $E_{1/2}$ of +0.845 V, strong methanol tolerant capability and remarkble stability for ORR. It also exhibits an efficient OER and HER electrocatalytic performance, with an overpotential of 314 mV and −192 mV at 10 mA cm^{-2} and outstanding durability, respectively. When applied in rechargeable Zn–air battery, the Co_9S_8@PNSC-based device displays high power density (203 mW cm^{-2}) and favorable charge–discharge reversibility with small variant of voltage gap after 12 h operation. The nanomaterial preparation strategy presented here may be expolited for the synthesis of high-performance electrocatalysts for diverse applications.

Declaration of Competing Interest

The authors declare no conflict of interest.

Credit authorship contribution statement

Xiaojing Zhu: Conceptualization, Methodology, Data curtion, Writing – original draft. **Qikai Wu:** Data curtion. **Jiale Dai:** Investigation. **Dengke Zhao:** Visualization. **Chenghao Yang:** Resources. **Ligui Li:** Writing – review & editing, Supervision, Funding acquisition. **Nanwen Li:** Resources. **Shaowei Chen:** Writing – review & editing, Supervision.

Acknowledgements

This work was financed by Natural Science Foundation of Guangdong Province (2019A1515011727); the Open Fund of the Guangdong Provincial Key Laboratory of Advance Energy Storage Materials; the National Key R&D Program of China (2018YFB1502600); and the Open Fund of Guangdong Provincial Key Laboratory of Petrochemical Pollution Process and Control, Guangdong University of Petrochemical Technology (No. 2018B030322017).

Supplementary materials

Supplementary material associated with this article can be found, in the online version, at doi:10.1016/j.electacta.2021.138299.

References

[1] I.C. Gerber, P. Serp, A theory/experience description of support effects in carbon-supported catalysts, Chem. Rev. 120 (2020) 1250–1349.
[2] Y. Peng, B. Lu, S. Chen, Carbon-supported single atom catalysts for electrochemical energy conversion and storage, Adv. Mater. 30 (2018) 1801995.
[3] M. Zhang, J. Chen, H. Li, P. Cai, Y. Li, Z. Wen, Ru-RuO_2/CNT hybrids as high--activity pH-universal electrocatalysts for water splitting within 0.73 V in an asymmetric-electrolyte electrolyzer, Nano Energy 61 (2019) 576–583.
[4] M. Yuan, Z. Sun, L. Lin, H. Yang, K.Yin D.Wang, C. Nan, G. Sun, H. Li, S. Ma, Atomically dispersed metal sites anchored in N-doped carbon nanosheets with enhanced Li storage performance, Mater. Chem. Front. 4 (2020) 2157–2167.
[5] Y. Chen, S. Ji, S. Zhao, W. Chen, J. Dong, W.-C. Cheong, R. Shen, X. Wen, L. Zheng, A.I. Rykov, S. Cai, H. Tang, Z. Zhuang, C. Chen, Q. Peng, D. Wang, Y. Li, Enhanced oxygen reduction with single-atomic-site iron catalysts for a zinc-air battery and hydrogen-air fuel cell, Nat. Commun. 9 (2018) 5422.
[6] X. Duan, N. Pan, C. Sun, K. Zhang, X. Zhu, M. Zhang, L. Song, H. Zheng, MOF-derived Co-MOF,O-doped carbon as trifunctional electrocatalysts to enable highly efficient Zn–air batteries and water-splitting, J. Energy Chem. 56 (2021) 290–298.
[7] L. Yan, H. Wang, J. Shen, J. Ning, Y. Zhong, Y. Hu, Formation of mesoporous Co/CoS/Metal-N-C@S, N-codoped hairy carbon polyhedrons as an efficient trifunctional electrocatalyst for Zn-air batteries and water splitting, Chem. Eng. J. 403 (2021) 126385.
[8] B.-Q. Li, C.-X. Zhao, S. Chen, J.-N. Liu, X. Chen, L. Song, Q. Zhang, Framework–porphyrin-derived single-atom bifunctional oxygen electrocatalysts and their applications in Zn–air batteries, Adv. Mater. 31 (2019) 1900592.
[9] H.-F. Wang, C. Tang, Q. Zhang, A review of precious-metal-free bifunctional oxygen electrocatalysts: rational design and applications in Zn−air batteries, Adv. Funct. Mater. 28 (2018) 1803329.
[10] A. Mahmood, H. Tabassum, R. Zhao, W. Guo, W. Aftab, Z. Liang, Z. Sun, R. Zou, Fe_2N/S/N codecorated hierarchical porous carbon nanosheets for trifunctional electrocatalysis, Small 14 (2018) 1803500.
[11] J. Wu, L. Hu, N. Wang, Y. Li, D. Zhao, L. Li, X. Peng, Z. Cui, L.-J. Ma, Y. Tian, X. Wang, Surface confinement assisted synthesis of nitrogen-rich hollow carbon cages with Co nanoparticles as breathable electrodes for Zn-air batteries, Appl. Catal. B: Environ. 254 (2019) 55–65.
[12] L. Zong, X. Chen, S. Liu, K. Fan, S. Dou, J. Xu, X. Zhao, W. Zhang, Y. Zhang, W. Wu, F. Lu, L. Cui, X. Jia, Q. Zhang, Y. Yang, J. Zhao, X. Li, Y. Deng, Y. Chen, L. Wang, Ultrafine Fe/Fe_3C decorated on Fe-N_x-C as bifunctional oxygen electrocatalysts for efficient Zn-air batteries, J. Energy Chem. 56 (2021) 72–79.
[13] Q. Wang, Y. Lei, Z. Chen, N. Wu, Y. Wang, B. Wang, Y. Wang, Fe/Fe_3C@C nanoparticles encapsulated in N-doped graphene–CNTs framework as an efficient bifunctional oxygen electrocatalyst for robust rechargeable Zn–air batteries, J. Mater. Chem. A 6 (2018) 516–526.
[14] Y. Pan, S. Liu, K. Sun, X. Chen, B. Wang, K. Wu, X. Cao, W.-C. Cheong, R. Shen, A. Han, Z. Chen, L. Zheng, J. Luo, Y. Lin, Y. Liu, D. Wang, Q. Peng, Q. Zhang, C. Chen, Y. Li, A Bimetallic Zn/Fe Polyphthalocyanine-derived single-atom Fe-N_4 catalytic site:a superior trifunctional catalyst for overall water splitting and Zn–Air batteries, Angew. Chem. Int. Ed. 57 (2018) 8614–8618.
[15] J. Long, Y. Gong, J. Lin, Metal–organic framework – derived Co_9S_8@CoS@CoO@C nanoparticles as efficient electro- and photo-catalysts for the oxygen evolution reaction, J. Mater. Chem. A 5 (2017) 10495–10509.
[16] H. Han, Z. Bai, T. Zhang, X. Wang, X. Yang, X. Ma, Y. Zhang, L. Yang, J. Lu, Hierarchical design and development of nanostructured trifunctional catalysts for electrochemical oxygen and hydrogen reactions, Nano Energy 56 (2019) 724–732.
[17] X. Zhu, J. Dai, L. Li, Z. Wu, S. Chen, N,S–Codoped hierarchical porous carbon spheres embedded with cobalt nanoparticles as efficient bifunctional oxygen electrocatalysts for rechargeable zinc-air batteries, Nanoscale 11 (2019) 21302–21310.
[18] M.-X. Chen, M. Zhu, M. Zuo, S.-Q. Chu, J. Zhang, Y. Wu, H.-W. Liang, X. Feng, Identification of catalytic sites for oxygen reduction in metal/nitrogen-doped carbons with encapsulated metal nanoparticles, Angew. Chem. Int. Ed. 59 (2020) 1627–1633.
[19] X. Zhao, X. Li, Y. Zhao, Z. Su, Y. Zhang, R. Wang, Facile synthesis of Tremelliform $Co_{0.85}Se$ nanosheets for supercapacitor, J. Alloy Compd. 697 (2017) 124–131.
[20] J. Zhu, Z. Nan, Zn-Doped Fe_3O_4 nanosheet formation induced by EDA with high magnetization and an investigation of the formation mechanism, J. Phys. Chem. C 121 (2017) 9612–9620.
[21] D. Deng, K.S. Novoselov, Q. Fu, N. Zheng, Z. Tian, X. Bao, Catalysis with two-dimensional materials and their heterostructures, Nat. Nanotechnol. 11 (2016) 218–230.
[22] H. Tao, Y. Gao, N. Talreja, F. Guo, J. Texter, C. Yan, Z. Sun, Two-dimensional nanosheets for electrocatalysis in energy generation and conversion, J. Mater. Chem. A 5 (2017) 7257–7284.
[23] C. Tan, X. Cao, X.-J. Wu, Q. He, J. Yang, X. Zhang, J. Chen, W. Zhao, S. Han, G.-H. Nam, M. Sindoro, H. Zhang, Recent advances in ultrathin two-dimensional nanomaterials, Chem. Rev. 117 (2017) 6225–6331.
[24] K. Qu, Y. Wang, A. Vasileff, Y. Jiao, H. Chen, Y. Zheng, Polydopamine-inspired nanomaterials for energy conversion and storage, J. Mater. Chem. A 6 (2018) 21827–21846.
[25] H. Xie, Y. Zhao, Y. Tian, X. Wang, M. Yan, Tailored synthesis from rhombic dodecahedron to spherical ordered mesoporous carbon nanoparticles via one-step strategy, Carbon 152 (2019) 295–304.

[26] Y. Yang, M. Yuan, H. Li, G. Sun, S. Ma, Controllable synthesis of ultrathin Co_9S_8 nanosheets as a highly efficient electrocatalyst for overall water splitting, Electrochim. Acta 281 (2018) 198–207.
[27] S.H. Lee, J. Kim, D.Y. Chung, J.M. Yoo, H.S. Lee, M.J. Kim, B.S. Mun, S.G. Kwon, Y.-E. Sung, T. Hyeon, Design principle of Fe–N–C electrocatalysts: how to optimize multimodal porous structures? J. Am. Chem. Soc. 141 (2019) 2035–2045.
[28] N. Wang, L. Li, D. Zhao, X. Kang, Z. Tang, S. Chen, Graphene composites with cobalt sulfide: efficient trifunctional electrocatalysts for oxygen reversible catalysis and hydrogen production in the same electrolyte, Small 13 (2017) 1701025.
[29] Y. Wang, L. Chen, Z. Mao, L. Peng, R. Xiang, X. Tang, J. Deng, Z. Wei, Q. Liao, Controlled synthesis of single cobalt atom catalysts via a facile one-pot pyrolysis for efficient oxygen reduction and hydrogen evolution reactions, Sci. Bull. 64 (2019) 1095–1102.
[30] Y.J. Sa, D.-J. Seo, J. Woo, J.T. Lim, J.Y. Cheon, S.Y. Yang, J.M. Lee, D. Kang, T.J. Shin, H.S. Shin, H.Y. Jeong, C.S. Kim, M.G. Kim, T.-Y. Kim, S.H. Joo, A general approach to preferential formation of active Fe–N_x Sites in Fe–N/C electrocatalysts for efficient oxygen reduction reaction, J. Am. Chem. Soc. 138 (2016) 15046–15056.
[31] R. Wu, J. Wang, K. Chen, S. Chen, J. Li, Q. Wang, Y. Nie, Y. Song, H. Chen, Z. Wei, Space-confined pyrolysis for the fabrication of Fe/N/C nanoparticles as a high performance oxygen reduction reaction electrocatalyst, Electrochim. Acta 244 (2017) 47–53.
[32] W. Zhang, Y. Huang, F. Yuan, B. Sun, J. Lin, J. Yang, D. Sun, Nitrogen-doped carbon nanofibers network derived from bacterial cellulose for the oxygen reduction reaction, Chem. Lett. 48 (2019) 1188–1191.
[33] A. Sadezky, H. Muckenhuber, H. Grothe, R. Niessner, U. Pöschl, Raman microspectroscopy of soot and related carbonaceous materials: spectral analysis and structural information, Carbon 43 (2005) 1731–1742.
[34] Y. Jia, L. Zhang, L. Zhuang, H. Liu, X. Yan, X. Wang, J. Liu, J. Wang, Y. Zheng, Z. Xiao, E. Taran, J. Chen, D. Yang, Z. Zhu, S. Wang, L. Dai, X. Yao, Identification of active sites for acidic oxygen reduction on carbon catalysts with and without nitrogen doping, Nat. Catal. 2 (2019) 688–695.
[35] L. Tao, M. Qiao, R. Jin, Y. Li, Z. Xiao, Y. Wang, N. Zhang, C. Xie, Q. He, D. Jiang, G. Yu, Y. Li, S. Wang, Bridging the surface charge and catalytic activity of a defective carbon electrocatalyst, Angew. Chem. Int. Ed. 58 (2019) 1019–1024.
[36] Q. Wang, Y. Ji, Y. Lei, Y. Wang, Y. Wang, Y. Li, S. Wang, Pyridinic-N-dominated doped defective graphene as a superior oxygen electrocatalyst for ultrahigh--energy-density Zn–air batteries, ACS Energy Lett. 3 (2018) 1183–1191.
[37] W. Niu, Z. Li, K. Marcus, L. Zhou, Y. Li, R. Ye, K. Liang, Y. Yang, Surface-modified porous carbon nitride composites as highly efficient electrocatalyst for Zn-Air Batteries, Adv. Energy Mater. 8 (2018) 1701642.
[38] L.-L. Ma, W.-J. Liu, X. Hu, P.K.S. Lam, J.R. Zeng, H.-Q. Yu, Ionothermal carbonization of biomass to construct sp^2/sp^3 carbon interface in N-doped biochar as efficient oxygen reduction electrocatalysts, Chem. Eng. J. 400 (2020) 125969.
[39] D. Guo, R. Shibuya, C. Akiba, S. Saji, T. Kondo, J. Nakamura, Active sites of nitrogen-doped carbon materials for oxygen reduction reaction clarified using model catalysts, Science 351 (2016) 361.
[40] N. Wang, B. Lu, L. Li, W. Niu, Z. Tang, X. Kang, S. Chen, Graphitic nitrogen is responsible for oxygen electroreduction on nitrogen-doped carbons in alkaline electrolytes: insights from activity attenuation studies and theoretical calculations, ACS Catal 8 (2018) 6827–6836.
[41] H.B. Yang, J. Miao, S.-F. Hung, J. Chen, H.B. Tao, X. Wang, L. Zhang, R. Chen, J. Gao, H.M. Chen, L. Dai, B. Liu, Identification of catalytic sites for oxygen reduction and oxygen evolution in N-doped graphene materials: development of highly efficient metal-free bifunctional electrocatalyst, Sci. Adv. 2 (2016) e1501122.
[42] W. Liu, D. Rao, J. Bao, L. Xu, Y. Lei, H. Li, Strong coupled spinel oxide with N-rGO for high-efficiency ORR/OER bifunctional electrocatalyst of Zn-air batteries, J. Energy Chem. (2020).
[43] Y. Lin, L. Yang, Y. Zhang, H. Jiang, Z. Xiao, C. Wu, G. Zhang, J. Jiang, L. Song, Defective carbon–CoP nanoparticles hybrids with interfacial charges polarization for efficient bifunctional oxygen electrocatalysis, Adv. Energy Mater. 8 (2018) 1703623.
[44] R. Zhao, Z. Liang, S. Gao, C. Yang, B. Zhu, J. Zhao, C. Qu, R. Zou, Q. Xu, Puffing up energetic metal–organic frameworks to large carbon networks with hierarchical porosity and atomically dispersed metal sites, Angew. Chem. Int. Ed. 58 (2019) 1975–1979.
[45] J. Dai, D. Zhao, W. Sun, X. Zhu, L.-J. Ma, Z. Wu, C. Yang, Z. Cui, L. Li, S. Chen, Cu(II) ions induced structural transformation of cobalt selenides for remarkable enhancement in oxygen/hydrogen electrocatalysis, ACS Catal. 9 (2019) 10761–10772.
[46] X. Hu, Y. Chen, M. Zhang, G. Fu, D. Sun, J.-M. Lee, Y. Tang, Alveolate porous carbon aerogels supported Co_9S_8 derived from a novel hybrid hydrogel for bifunctional oxygen electrocatalysis, Carbon 144 (2019) 557–566.
[47] Y. Zhang, S. Chao, X. Wang, H. Han, Z. Bai, L. Yang, Hierarchical Co_9S_8 hollow microspheres as multifunctional electrocatalysts for oxygen reduction, oxygen evolution and hydrogen evolution reactions, Electrochim. Acta 246 (2017) 380–390.
[48] P. Zhang, D. Bin, J.-S. Wei, X.-Q. Niu, X.-B. Chen, Y.-Y. Xia, H.-M. Xiong, Efficient oxygen electrocatalyst for Zn–air batteries: carbon dots and Co_9S_8 nanoparticles in a N,S-codoped carbon matrix, ACS Appl. Mater. Inter. 11 (2019) 14085–14094.
[49] H. Li, Z. Guo, X. Wang, Atomic-layer-deposited ultrathin Co_9S_8 on carbon nanotubes: an efficient bifunctional electrocatalyst for oxygen evolution/reduction reactions and rechargeable Zn–air batteries, J. Mater. Chem. A 5 (2017) 21353–21361.
[50] J. Bai, T. Meng, D. Guo, S. Wang, B. Mao, M. Cao, Co_9S_8@MoS_2 core–shell heterostructures as trifunctional electrocatalysts for overall water splitting and Zn–Air batteries, ACS Appl. Mater. Inter. 10 (2018) 1678–1689.
[51] N. Jia, J. Liu, Y. Gao, P. Chen, X. Chen, Z. An, X. Li, Y. Chen, Graphene-encapsulated Co_9S_8 nanoparticles on N,S-codoped carbon nanotubes: an efficient bifunctional oxygen electrocatalyst, Chem. Sus. Chem. 12 (2019) 3390–3400.
[52] C. Hu, L. Zhang, J. Gong, Recent progress made in the mechanism comprehension and design of electrocatalysts for alkaline water splitting, Energy Environ. Sci. 12 (2019) 2620–2645.
[53] Z. Sun, X. Wang, M. Yuan, H. Yang, Y. Su, K. Shi, C. Nan, H. Li, G. Sun, J. Zhu, X. Yang, S. Chen, Lewis base-hungry" amorphous–crystalline nickel borate–nickel sulfide heterostructures by in situ structural engineering as effective bifunctional electrocatalysts toward overall water splitting, ACS Appl. Mater. Interfaces 12 (2020) 23896–23903.
[54] H. Liu, C.-Y. Xu, Y. Du, F.-X. Ma, Y. Li, J. Yu, L. Zhen, Ultrathin Co9S8 nanosheets vertically aligned on N,S/rGo for low voltage electrolytic water in alkaline media, Sci. Rep. 9 (2019) 1951.
[55] S. Zhang, D. Zhai, T. Sun, A. Han, Y. Zhai, W.-C. Cheong, Y. Liu, C. Su, D. Wang, Y. Li, In situ embedding Co9S8 into nitrogen and sulfur codoped hollow porous carbon as a bifunctional electrocatalyst for oxygen reduction and hydrogen evolution reactions, Appl. Catal. B: Environ. 254 (2019) 186–193.
[56] N. Jia, J. Liu, Y. Gao, P. Chen, X. Chen, Z. An, X. Li, Y. Chen, Graphene-encapsulated Co9S8 nanoparticles on N,S-codoped carbon nanotubes: an efficient bifunctional oxygen electrocatalyst, Chem. Sus. Chem. 12 (2019) 3390–3400.
[57] Z.-Q. Cao, M.-Z. Wu, H.-B. Hu, G.-J. Liang, C.-Y. Zhi, Monodisperse Co9S8 nanoparticles in situ embedded within N, S-codoped honeycomb-structured porous carbon for bifunctional oxygen electrocatalyst in a rechargeable Zn–air battery, NPG Asia Mater. 10 (2018) 670–684.
[58] W. Li, Y. Li, H. Fu, G. Yang, Q. Zhang, S. Chen, F. Peng, Phosphorus doped Co_9S_8@CS as an excellent air-electrode catalyst for zinc-air batteries, Chem. Eng. J. 381 (2020) 122683.